

The Role of Ligand Acid–Base Reaction in the Facile Synthesis of Alkali Metal Neodymium Penta- and Heptafluoride Nanocrystals

Xiangyang Wu, Jing Yang Tham, Ann-Marie Chacko, and Edwin K. L. Yeow*



Cite This: *Chem. Mater.* 2021, 33, 8367–8377



Read Online

ACCESS |



Metrics & More

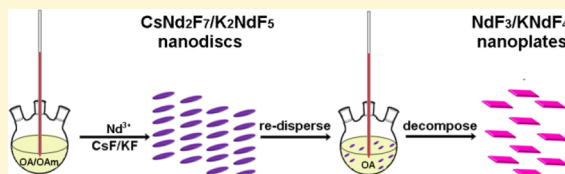


Article Recommendations



Supporting Information

ABSTRACT: We report a facile co-precipitation method of synthesizing orthorhombic phase CsNd_2F_7 and hexagonal phase K_2NdF_5 nanocrystals, which avoids the use of relatively harsh conditions (e.g., high temperatures and long reaction times in hydrothermal synthesis). By reacting MF (M = Cs and K), $\text{Nd}(\text{CH}_3\text{CO}_2)_3$, oleic acid (OA), and 1-octadecene in the presence of sufficient amounts of oleylamine ligands (OAm) to ensure a non-acidic environment, CsNd_2F_7 and K_2NdF_5 nanocrystals are formed for reaction temperatures (T_r) ranging between 150 and 300 °C. When OAm is in excess of OA and $T_r = 300$ °C, uniformly distributed CsNd_2F_7 nanodiscs (~ 20 nm in diameter) and sub-10 nm K_2NdF_5 nanodiscs with an average thickness of 2–3 unit cell layers are formed. When OAm is removed, the acidic mixture produces CsNd_2F_7 nanocrystals at low T_r (150–200 °C); however, a mixture of NdF_3 and Cs-oleate is observed instead when T_r is increased. Similarly, in an acidic environment, K_2NdF_5 nanocrystals rapidly decompose into a mixture of $\text{K}_{0.156}\text{Nd}_{0.142-y}\text{F}_{0.702-3y}$ and $y(\text{NdF}_3)$ ($y < 0.142$) at low T_r (150–200 °C), while orthorhombic KNdF_4 nanocrystals are synthesized at higher T_r (>200 °C). Therefore, the penta- and heptafluoride nanocrystals are thermodynamically stable only in a basic medium when OA is consumed, in part by its condensation reaction with OAm. We further demonstrate that the CsNd_2F_7 and K_2NdF_5 nanocrystals display good light-to-heat conversion efficiencies (16–27%) and computed tomography (CT) attenuation, making them promising theranostic photothermal imaging/therapy and CT contrast agents.



INTRODUCTION

Alkali metal rare earth metal tetrafluoride nanocrystals have attracted a significant amount of attention due to their wide ranging applications in lasing material technology, anti-counterfeiting security, and medical diagnosis and therapy.^{1–3} While different types of lanthanide ions have been utilized, neodymium is one of the most attractive elements to incorporate into a tetrafluoride nanocrystal.^{4,5} When a system composed of a low phonon energy tetrafluoride matrix doped with small amounts of Nd^{3+} (e.g., $\text{NaYF}_4:\text{Nd}^{3+}$ (1 mol %)) is irradiated with an 808 nm light, the lanthanide ions absorb strongly and emit downconversion luminescence in the second window near-infrared (NIR) region (NIR-II, 900–1700 nm). This is highly advantageous in biomedical imaging since an 808 nm laser source is commonly available and the light is able to penetrate deeper into tissues.⁶ Furthermore, due to the low absorption of 808 nm light by water, overheating of biological samples is avoided.⁷ In the presence of other co-doped lanthanide ions such as Yb^{3+} and Er^{3+} , Nd^{3+} -sensitized $\text{NaYF}_4:\text{Nd}^{3+}/\text{Yb}^{3+}/\text{Er}^{3+}$ nanocrystal converts NIR excitation light (i.e., 808 nm) to ultraviolet (UV) and visible emission light. Recently, upconversion nanocrystals were used to activate UV–visible absorbing photocatalysts via an upconverted photon energy transfer process to induce chemical reactions (e.g., photo-oxidation).⁸

A group of tetrafluorides that contain neodymium as the only rare earth (RE) element (e.g., NaNdF_4 and KNdF_4) is found to undergo efficient light-to-heat conversion.^{9,10} In these

systems, the Nd^{3+} ions are packed close to each other such that a photoexcited Nd^{3+} ion and a neighboring unexcited Nd^{3+} ion undergo cross-relaxation to their $^4\text{I}_{15/2}$ state before generating heat via a non-radiative relaxation to the $^4\text{I}_{9/2}$ ground state.^{11,12} The most commonly studied alkali metal neodymium tetrafluoride is NaNdF_4 .^{9,13} One of our groups has exploited the photothermal properties of NaNdF_4 nanorods in anti-counterfeiting applications.⁹ Ding *et al.* have also studied the efficacy of photothermal therapy against tumour using NaNdF_4 nanoparticles.¹³ Recently, ultrathin rectangular-like KNdF_4 nanoplates were used for near-quantitative cyanosilylation of ketones synthesized by combining their photothermal property and the Lewis-acid catalytic activity of Nd^{3+} .¹⁰

Apart from their ability to convert light to heat, suggesting that MNdF_4 nanocrystals are suitable for use in photothermal imaging and therapy, the tetrafluoride nanomaterials may also act as good computed tomography (CT) contrast agents. This is due to their high atomic number and optimal K-edge that falls within the energy range of the X-ray spectrum suitable for medical imaging systems as demonstrated by a series of

Received: August 9, 2021

Revised: October 13, 2021

Published: October 26, 2021



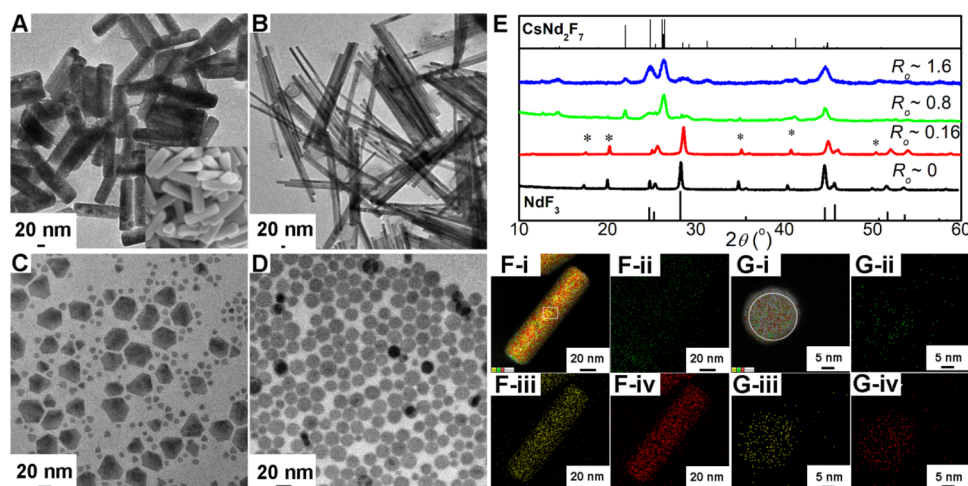


Figure 1. Nanocrystals formed using CsF as an alkali metal precursor, $R_M = 4.0$ and $T_r = 300$ °C. (A–D) TEM images of nanocrystals synthesized using different R_o values (A: $R_o = 0$; B: $R_o = 0.16$; C: $R_o = 0.8$; and D: $R_o = 1.6$). The SEM image in inset of (A) illustrates the cross-section of the nanorods. (E) XRD patterns of nanocrystals synthesized using different R_o values. Standard XRD patterns of hexagonal phase NdF_3 (PDF no. 00-09-0416) and orthorhombic phase CsNd_2F_7 (PDF no. 00-053-0994) are provided. Peaks labeled with an asterisk (*) are from Cs-oleate (Figure S5, Supporting Information). HAADF-STEM-correlated EDS elemental mapping images of a single (F) NdF_3 nanorod ($R_o = 0$) and (G) CsNd_2F_7 nanodisc ($R_o = 1.6$). The area analyzed for each nanocrystal in EDS is given within the highlighted boxes in F-i and G-i. (F-i, G-i) Overlay images of (ii), (iii), and (iv), (F-ii, G-ii) Cs L-edge, (F-iii, G-iii) Nd L-edge, and (F-iv, G-iv) F K-edge.

lanthanide-based tetrafluorides, including NaNdF_4 .^{13–17} The attenuation coefficient is further enhanced when (1) the proportion of lanthanide ions in single nanocrystals is increased and (2) an alkali metal with a higher atomic number is used (e.g., Cs vs Na).^{18,19}

The morphology and crystalline phase of NaNdF_4 nanocrystals have been reported to be dependent on the type of precursor/ligand and reaction conditions (e.g., temperature) used.^{20–26} In particular, the effects of environment acidity on the stability of the different crystalline phases of NaNdF_4 have been discussed.^{21,22} While reports on the synthesis and applications of Nd^{3+} -based tetrafluoride nanocrystals are relatively common, investigations on the preparation and characterization of alkali metal neodymium pentafluoride and heptafluoride compounds (e.g., CsNd_2F_7 and K_2NdF_5) are scarce. In terms of the preparation of these nanostructures, hydrothermal synthesis involving the reaction between an alkali metal halide (e.g., CsF or KF) and a Nd precursor (e.g., Nd_2O_3 , NdF_3) at high temperatures (e.g., >400 °C) and for long reaction times (e.g., a few days) is the most commonly employed method.^{27–31} It is worth noting that the synthesis of pure CsNdF_4 is challenging, and phase diagrams suggest that neodymium pentafluorides containing Na^+ and Cs^+ are likely unstable and hence difficult to prepare.³²

In this study, a facile co-precipitation method using MF ($M = \text{Cs}$ and K) as the alkali metal precursor is used to prepare CsNd_2F_7 and K_2NdF_5 nanocrystals without the need for harsh experimental conditions (e.g., high reaction temperature and long reaction time). The effects of lowering the acidity of the medium, through a combination of the coordinating ligands oleic acid (OA) and oleylamine (OAm), on the evolution of formation and stability of the final product are examined. The photothermal and NIR luminescence efficiencies of CsNd_2F_7 and K_2NdF_5 nanocrystals are also characterized. As proof-of-concept, assessment of CsNd_2F_7 , K_2NdF_5 , and NaNdF_4 nanocrystals for use as CT contrast agents was compared against iohexol ($\text{C}_{19}\text{H}_{26}\text{I}_3\text{N}_3\text{O}_9$), a typical iodine-based CT contrast agent.^{33,34} Given that the X-ray mass attenuation

coefficient of Nd at 50 keV ($\sim 16.50 \text{ cm}^2 \text{ g}^{-1}$) is larger than that of I ($\sim 12.32 \text{ cm}^2 \text{ g}^{-1}$), we have set out to explore whether the Nd^{3+} -based nanocrystals synthesized in this work display better attenuation as compared to iohexol.

RESULTS AND DISCUSSION

CsF Alkali Metal Precursor. The nanocrystals were synthesized by a co-precipitation method by first reacting $\text{Nd}(\text{CH}_3\text{CO}_2)_3$ in an OA-ODE solvent before the addition of either the desired alkali metal fluoride MF ($M = \text{Cs}$, K , or Na) or a mixture of MF and OAm. We begin with CsF and discuss the nanocrystals formed at a reaction temperature of $T_r = 300$ °C (see the Experimental Section for details). The transmission electron microscopy (TEM) images of the final products formed for a fixed MF ($M = \text{Cs}$) mol %: Nd^{3+} mol % ratio of $R_M = 4.0$ and various OAm mol %:OA mol % ratios ($R_o = 0, 0.16, 0.8$, and 1.6) (see Table S1, Supporting Information, for the exact OAm and OA composition for each R_o) are given in Figure 1. When $R_o = 0$ (i.e., absence of OAm), the final product obtained are nanorods with average length (L) = 132.3 ± 8.0 nm and width (W) = 34.8 ± 1.7 nm (Figure 1A with inset displays the scanning electron microscopy (SEM) image. Size distributions are presented in Figure S1, Supporting Information.) The crystalline phase of the nanorods is characterized using X-ray diffraction (XRD), and the observed peaks match those of the standard hexagonal phase NdF_3 (PDF no. 00-09-0416) (Figure 1E). Furthermore, high-angle annular dark field scanning transmission electron microscopy (HAADF-STEM)-correlated energy-dispersive X-ray spectroscopy (EDS) elemental mappings of individual nanorods show that Nd and F are the two main elements present (Figure 1F). The average atomic ratio of F^- to Nd^{3+} within four separate areas of the nanorod in Figure 1F is determined to be $\sim 2.7 \pm 0.4$ (Figure S2, Supporting Information), in agreement with the $\text{F}^-:\text{Nd}^{3+}$ stoichiometric ratio in NdF_3 . On the average, the amount of Cs detected is <1%. The assignment to hexagonal phase NdF_3 is further supported by the (002) lattice plane with lattice distance =

0.36 nm in the high-resolution TEM (HRTEM) image, corresponding to the $2\theta = 24.9^\circ$ peak in the XRD pattern (Figure S3A, Supporting Information). When a small amount of OAm is added into the reaction mixture such that R_0 is increased to 0.16, significantly longer nanorods with $\langle L \rangle = 538.6 \pm 42.7$ nm and $\langle W \rangle = 20.4 \pm 8.1$ nm are obtained (Figure 1B and size distributions shown in Figure S4, Supporting Information). The XRD peaks of the ultralong nanorods are again well indexed to the peaks of standard hexagonal NdF_3 (Figure 1E).

Apart from the diffraction peaks associated with NdF_3 , extra peaks at $2\theta = 17.4, 20.0, 35.1, 40.5,$ and 49.9° are also observed in the XRD spectra for $R_0 = 0$ and 0.16 (peaks denoted by * in Figure 1E). In order to establish the origin of these peaks, caesium oleate (Cs-oleate) is first prepared by reacting CsF with OA. The product is characterized using nuclear magnetic resonance (NMR) (Figure S5A, Supporting Information), and the XRD pattern of the as-prepared Cs-oleate is presented in Figure S5B, Supporting Information. Clearly, the additional peaks labeled with * in Figure 1E are attributed to Cs-oleate produced *via* the reaction between OA/ $\text{Nd}(\text{oleate})_3$ and CsF during the synthesis of the nanorods. It is worth noting that the peak at $2\theta = 28.4^\circ$ of Cs-oleate (Figure S5B, Supporting Information) overlaps with the peak corresponding to the (111) lattice plane of NdF_3 .

The TEM image of the product obtained when the concentration of OAm is close to that of OA ($R_0 = 0.8$) indicates the existence of both large and small nanocrystals (Figure 1C). When the concentration of OAm is in excess of OA ($R_0 = 1.6$), uniform nanodiscs with average diameter $\langle D \rangle = 18.9 \pm 2.3$ nm and average thickness $\langle l \rangle = 9.1 \pm 0.7$ nm are obtained (Figure 1D and Figure S6, Supporting Information). For $R_0 = 0.8$ and 1.6, the XRD peaks of the nanostructures match the diffraction peaks of standard orthorhombic phase CsNd_2F_7 (PDF no. 00-053-0994) (Figure 1E). The assignment to orthorhombic phase CsNd_2F_7 nanocrystals prepared under $R_0 = 1.6$ is further supported by the (022) or (040) lattice plane with lattice distance = 0.35 nm in the HRTEM image of a single nanodisc standing on its edge (corresponding to the $2\theta = 29.3^\circ$ peak in the XRD pattern), and the (002) or (031) lattice plane with lattice distance = 0.40 nm in the HRTEM image of a nanodisc laying on its base (corresponding to the $2\theta = 22.1^\circ$ peak in the XRD pattern) (Figure S3B, Supporting Information). The crystal growth occurs *via* the deposition of precursors onto the CsNd_2F_7 crystals with increasing reaction time (Text S3.1, Supporting Information).

In addition, the diffraction peaks arising from Cs-oleate are no longer apparent, suggesting its complete consumption. HAADF-STEM-correlated EDS elemental mapping of individual nanodiscs synthesized using $R_0 = 1.6$ reveals the presence of the elements Cs, Nd, and F with an atomic ratio of $\text{Cs}^+:\text{Nd}^{3+}:\text{F}^- = 8.4\%:21.6\%:70.0\%$ (Figure 1G and Figure S7, Supporting Information), close to the stoichiometric $\text{Cs}^+:\text{Nd}^{3+}:\text{F}^-$ ratio in CsNd_2F_7 (*i.e.*, 10%:20%:70%).

Changes in the morphology and crystalline phase of the product with different R_0 values are also observed for a smaller concentration of CsF (*i.e.*, $R_M = 3.0$). For example, hexagonal phase NdF_3 nanorods with $\langle L \rangle = 58.5 \pm 9.5$ nm and $\langle W \rangle = 17.0 \pm 5.7$ nm are obtained in the absence of OAm (Figure S8, Supporting Information). On the other hand, when $R_0 = 1.6$, irregular-shaped orthorhombic phase CsNd_2F_7 nanocrystals with sharp edges are formed (Figure S8, Supporting Information). The above results demonstrate that for $T_r =$

300°C , hexagonal phase NdF_3 nanorods are produced in the absence or presence of small amounts of OAm (*e.g.*, $R_0 = 0$ and 0.16) whereas orthorhombic phase CsNd_2F_7 nanocrystals are observed at much higher OAm concentrations (*e.g.*, $R_0 = 0.8$ and 1.6).

Effects of Reaction Temperature. The effects of the reaction temperature T_r on the morphology and phase of the nanocrystals are examined next. We focus on two scenarios: (i) when OAm is absent ($R_0 = 0$) and (ii) when the concentration of OAm is in excess of OA ($R_0 = 1.6$). When $R_0 = 0$, $R_M = 4.0$, and $T_r = 162^\circ\text{C}$, poorly separated worm-like nanostructures are observed in the TEM image (Figure S9, Supporting Information). When T_r is increased to 202 and 274°C , sub-10 nm nanoparticles with average diameter $\langle D \rangle = 4.8 \pm 1.0$ nm (Figure 2A and Figure S10, Supporting Information) and

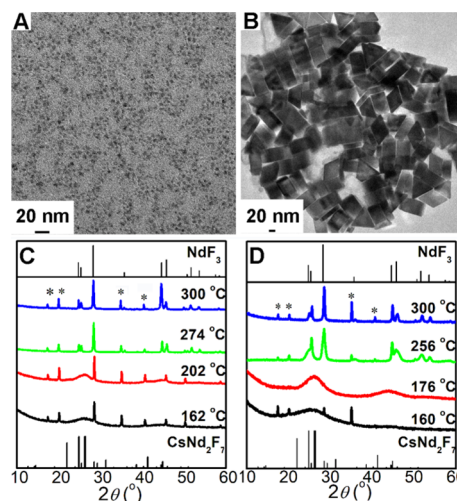


Figure 2. Nanocrystals formed with CsF as an alkali metal precursor in an OA-ODE solvent without OAm ($R_0 = 0$). TEM images of nanocrystals synthesized for $R_M = 4.0$ and $T_r =$ (A) 202°C and (B) 274°C . XRD patterns of nanocrystals synthesized for different T_r values and $R_M =$ (C) 4.0 and (D) 3.0. Standard XRD patterns of hexagonal phase NdF_3 (PDF no. 00-09-0416) and orthorhombic phase CsNd_2F_7 (PDF no. 00-053-0994) are also included. Peaks labeled with an asterisk (*) are from Cs-oleate (Figure S5, Supporting Information).

irregular-shaped nanosheets (Figure 2B) are obtained, respectively. Increasing T_r further to 300°C results in the formation of hexagonal phase NdF_3 nanorods as discussed above in Figure 1A. Similar morphology changes in the nanocrystals for $R_M = 3.0$ and $R_0 = 0$ are also observed; ultrasmall nanocrystals are formed at low reaction temperatures (*e.g.*, $T_r = 160$ and 176°C), nanosheets at intermediate temperatures (*e.g.*, $T_r = 256^\circ\text{C}$), and NdF_3 nanorods at $T_r = 300^\circ\text{C}$ (Figures S11 and S8, Supporting Information).

The crystalline phase of the nanocrystals formed at various T_r values when $R_0 = 0$ is characterized using XRD (Figure 2C for $R_M = 4.0$ and Figure 2D for $R_M = 3.0$). For T_r below *ca.* 202°C , the XRD pattern exhibits two broad peaks at $2\theta = 26.0$ and 44.4° . This suggests that the as-prepared nanocrystals are amorphous with low crystallinity quality. In addition, diffraction peaks ascribed to Cs-oleate are also seen except in the XRD spectrum for $R_M = 3.0$ and $T_r = 176^\circ\text{C}$. The broad peaks overlap with the diffraction peaks of CsNd_2F_7 and NdF_3 , making an accurate assignment of either phase to the nanocrystals using XRD analysis difficult. Therefore, SEM-

correlated EDS experiment was performed on the nanoparticles obtained for $R_M = 3$, $R_o = 0$, and $T_r = 176$ °C where the contribution from Cs-oleate is minimal. In this case, the EDS spectrum collected for a relatively large area of the sample ($\sim 39.9 \mu\text{m} \times 21.5 \mu\text{m}$) shows the presence of the elements Cs, Nd, and F (Figure S12, Supporting Information). The percentage of Cs is significant at 16.9%, suggesting that the nanoparticles formed are most likely CsNd_2F_7 . To further support this assignment, HAADF-STEM-correlated EDS point analysis was performed on single nanocrystals. The average atomic $\text{Cs}^+:\text{Nd}^{3+}:\text{F}^-$ ratio, based on four separate points on different nanocrystals, is $12.9 \pm 5.2\%:23.3 \pm 3.4\%:63.8 \pm 7.9\%$, which is close to the stoichiometric ratio in CsNd_2F_7 (Figure S13, Supporting Information). Furthermore, a lattice displacement of ~ 0.34 nm, attributed to the (231) lattice plane of orthorhombic phase CsNd_2F_7 , is resolved from the HRTEM image (Figure S13, Supporting Information) of a single nanocrystal. Therefore, at low reaction temperatures, orthorhombic phase CsNd_2F_7 nanocrystals are produced.

On the other hand, XRD patterns recorded for nanocrystals synthesized at higher reaction temperatures and $R_o = 0$ show the formation of hexagonal phase NdF_3 along with Cs-oleate ($T_r > 202$ °C in Figure 2C,D). We propose that during the reaction, CsNd_2F_7 nanocrystals are formed at low T_r . On the other hand, at higher reaction temperatures, NdF_3 and Cs-oleate are formed in a binary OA-ODE solvent mixture due most likely to the decomposition of CsNd_2F_7 nanocrystals formed at low temperatures when the reaction temperature is elevated: $\text{CsNd}_2\text{F}_7 + \text{OA} \rightarrow \text{NdF}_3 + \text{Cs-oleate} + \text{F}^-$. This is further supported when we investigated the effects of T_r on the phase of the nanocrystals formed in the presence of OAm as discussed below.

The size of the nanocrystals formed for $R_M = 4.0$ and $R_o = 1.6$ increases with T_r (i.e., average diameter $\langle D \rangle = 4.6 \pm 0.6$, 10.2 ± 1.2 , 16.9 ± 3.3 , and 18.9 ± 2.3 nm for $T_r = 164$, 238, 278, and 300 °C, respectively) (Figure 3A,B and Figure S14, Supporting Information). A similar trend is also observed for $R_M = 3.0$ and $R_o = 1.6$ (Figure S15, Supporting Information). The XRD patterns collected for low reaction temperatures when $R_o = 1.6$ (i.e., $R_M = 4.0$ and $T_r = 164$ °C in Figure 3C, and $R_M = 3.0$ and $T_r = 160$ and 180 °C in Figure 3D) closely resemble those of orthorhombic phase CsNd_2F_7 nanocrystals formed at approximately similar temperatures in the absence of OAm ($R_o = 0$) (e.g., $\lesssim 200$ °C in Figure 2C,D). In order to further ascertain that CsNd_2F_7 nanocrystals are formed at a low temperature when $R_o = 1.6$, the SEM-correlated EDS spectrum is recorded for the nanocrystals formed for $R_M = 3.0$ and $T_r = 180$ °C (Figure S16, Supporting Information). The averaged ratio of $\text{Cs}^+:\text{Nd}^{3+}:\text{F}^-$ is determined to be $14.4 \pm 0.3\%:19.7 \pm 0.4\%:65.9 \pm 0.5\%$, which is close to the theoretical ratio of 10%:20%:70%. Interestingly, unlike the case for $R_o = 0$, it is observed that in the presence of a large amount of OAm, orthorhombic phase CsNd_2F_7 nanocrystals are formed regardless of the reaction temperature employed here as noted from the XRD patterns for $T_r > 200$ °C in Figure 3C,D. In addition, the XRD peaks appear to become sharper with increasing T_r , suggesting an improvement in crystallinity with reaction temperature.

We note that the diffraction peaks of Cs-oleate can be found in the XRD patterns when the reaction temperature is low for both $R_o = 0$ and 1.6 (e.g., $T_r \approx 160$ – 165 °C in Figures 2C,D, 3C,D). This is because of the presence of unreacted Cs-oleate, formed from the reaction between CsF and OA, which is not

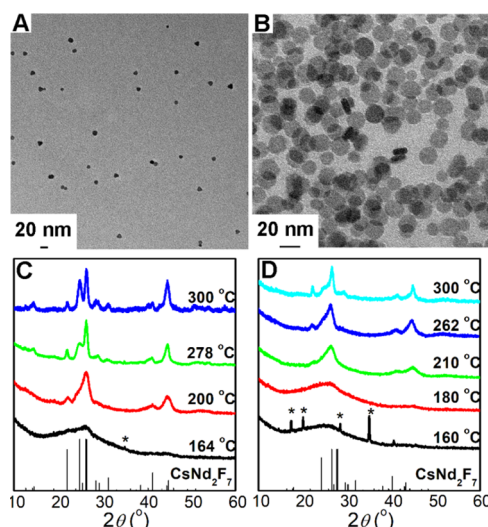


Figure 3. Nanocrystals formed with a CsF alkali metal precursor in an OA-OAm-ODE solvent ($R_o = 1.6$). TEM images of nanocrystals synthesized for $R_M = 4.0$ and $T_r =$ (A) 238 °C and (B) 278 °C. XRD patterns of nanocrystals synthesized for different T_r values and $R_M =$ (C) 4.0 and (D) 3.0. The standard XRD pattern of orthorhombic phase CsNd_2F_7 (PDF no. 00-053-0994) is included. Peaks labeled with an asterisk (*) are from Cs-oleate (Figure S5, Supporting Information).

soluble in the solvents used to wash the as-prepared nanocrystals (e.g., ethanol and cyclohexane). On the other hand, unreacted $\text{Nd}(\text{oleate})_3$ is soluble in cyclohexane and is most likely removed during the washing process (Figure S17, Supporting Information). For $R_M = 3.0$, the majority of Cs-oleate is consumed at a reaction temperature *ca.* 176–180 °C (Figures 2D and 3D). When $R_o = 1.6$, neither NdF_3 nor Cs-oleate are detected in the XRD patterns for higher reaction temperatures (e.g., $T_r > 200$ °C) (Figure 3C,D). Therefore, in the presence of excess OAm, the as-prepared CsNd_2F_7 nanocrystals remain relatively stable against thermal decomposition to NdF_3 and Cs-oleate. Table S2, Supporting Information, provides a summary of the nanocrystals formed under various preparation conditions.

Ligand Acid–Base Reaction. The acid–base reaction between OA and OAm plays an important role in determining the stability of the CsNd_2F_7 nanocrystals. At room temperature, in a mixture of OA and OAm, deprotonation of OA and protonation of the amine group in OAm result in the formation of an oley–oleic complex (i.e., $\text{CH}_3(\text{CH}_2)_7\text{CH}=\text{CH}(\text{CH}_2)_7\text{CH}_2\text{NH}_3^+\cdots^-\text{OOC}(\text{CH}_2)_7\text{CH}=\text{CH}(\text{CH}_2)_7\text{CH}_3$).^{35–37} The ^1H NMR signal of the $\alpha\text{-CH}_2$ resonances of neat OAm in CDCl_3 (~ 2.646 ppm) undergoes a gradual downfield shift with decreasing R_o (2.696, 2.739, and 2.867 ppm for $R_o = 1.6$, 0.8, and 0.16, respectively) (Figure 4A and Figure S18A–E, Supporting Information for the full NMR spectra). This is due to a proton transfer from OA resulting in the protonation of OAm.³⁷ Concomitantly, the $\alpha\text{-CH}_2$ resonances of neat OA in CDCl_3 at ~ 2.343 ppm experience an upfield shift to 2.227, 2.104, and 2.091 ppm for $R_o = 0.16$, 0.8, and 1.6, respectively (Figure 4A). The observed shift with increasing R_o is attributed to a greater extent of the deprotonation of OA as the proportion of OAm is increased.^{38,39} As discussed previously, an increase in deprotonation of the carboxylic acid leads to reduction in the acidity of the reaction medium.^{21,22,39}

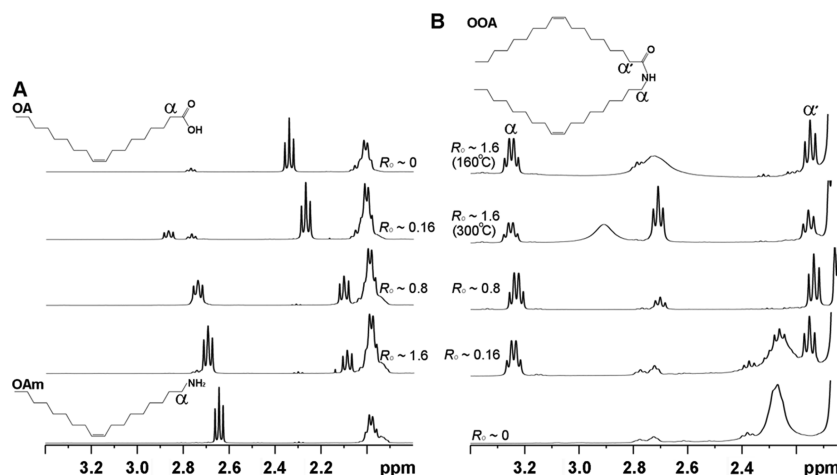


Figure 4. (A) ^1H NMR spectra of neat OA (top panel), neat OAm (bottom panel), and a mixture of OAm and OA ($R_0 = 0.16, 0.8$, and 1.6) reacted at room temperature. (B) ^1H NMR spectra of the reaction mixtures for $R_M = 4.0$ and $R_0 = 0, 0.16, 0.8$, and 1.6 ($T_r = 300\text{ }^\circ\text{C}$) and $R_M = 4.0$ and $R_0 = 1.6$ ($T_r = 160\text{ }^\circ\text{C}$). The full ^1H NMR spectra are shown in Figure S18, Supporting Information.

The ^1H NMR spectra of the resulting solution used to prepare the nanocrystals for $R_M = 4.0$, $T_r = 300\text{ }^\circ\text{C}$, and $R_0 = 0, 0.16, 0.8$, and 1.6 , and $R_M = 4.0$, $T_r = 160\text{ }^\circ\text{C}$ and $R_0 = 1.6$ were also recorded in CDCl_3 (Figure 4B and Figure S18F–J, Supporting Information for the full NMR spectra). For $T_r = 300\text{ }^\circ\text{C}$ and $R_0 = 0$, the chemical shift of the $\alpha\text{-CH}_2$ resonances of unreacted OA occurs at 2.269 ppm , a slight upfield shift compared to neat OA in CDCl_3 in Figure 4A. The amount of unreacted OA remaining in the solution is calculated to be *ca.* 8.35 mmol (see Text S3.2, Supporting Information). Upon the addition of OAm, the characteristic ^1H NMR peaks of neutral *N*-(*cis*-9-octadecenyl)oleamide (OOA), formed during the condensation reaction at a sufficiently elevated temperature, are observed at 3.240 ppm ($\alpha\text{-CH}_2$ resonances of OOA) and 2.150 ppm ($\alpha'\text{-CH}_2$ resonances of OOA) (Figure 4B).⁴⁰ For $T_r = 300\text{ }^\circ\text{C}$ and $R_0 = 0.16$, the ^1H NMR peak of unreacted OA is still observed; however, the amount of free OA ligand is reduced to *ca.* 2.87 mmol (Text S3.2, Supporting Information). When R_0 is increased to 0.8 and 1.6 , the ^1H NMR peak of OA is no longer detectable, indicating the complete consumption of the ligand. Furthermore, the ^1H NMR peak of free OAm at 2.7 ppm is observed. The above results clearly show that the reaction environment is acidic for $R_0 = 0$ or 0.16 and basic for $R_0 = 0.8$ or 1.6 .

Based on the above findings, the following mechanism is proposed. CsNd_2F_7 nanocrystals are formed at low temperatures (*e.g.*, $\lesssim 200\text{ }^\circ\text{C}$). However, in the absence of OAm ($R_0 = 0$) or when $R_0 = 0.16$, CsNd_2F_7 nanocrystals in an OA-ODE binary solvent become unstable in the acidic medium at high reaction temperatures and undergo decomposition to NdF_3 and Cs-oleate (Figure 2). On the other hand, when OAm is present in sufficient amounts (*e.g.*, $R_0 = 0.8$ and 1.6) such that the acidity of the reaction medium is significantly reduced, CsNd_2F_7 nanocrystals are thermodynamically stable and resistant against transformation to NdF_3 and Cs-oleate even at high reaction temperatures (Figure 3).

The decomposition of CsNd_2F_7 nanocrystals in an acidic environment at a high temperature is further supported by a control experiment where orthorhombic phase CsNd_2F_7 nanodiscs are first prepared before redispersing in a binary OA-ODE solvent and aged at $300\text{ }^\circ\text{C}$ for 120 min . The final product obtained is hexagonal phase NdF_3 nanosheets,

demonstrating the decomposition of CsNd_2F_7 to NdF_3 (Figure 5). This is further supported by HAADF-STEM-correlated

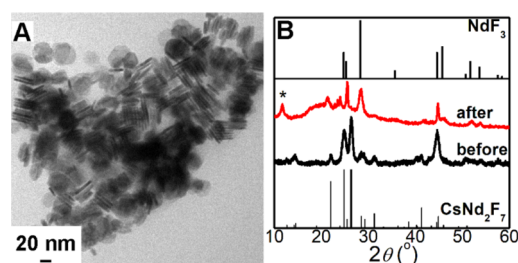


Figure 5. (A) TEM image and (B) XRD pattern of the nanocrystals obtained after (red) heating CsNd_2F_7 nanocrystals in a mixture of ODE (7 mL) and OA (3 mL) for 120 min at $300\text{ }^\circ\text{C}$. The peak labeled with an asterisk (*) is from Cs-oleate (Figure S5, Supporting Information). The XRD pattern of CsNd_2F_7 nanocrystals before treatment is also given (black).

EDS elemental mapping analysis that shows that the amount of Cs in the nanocrystals after aging is negligible and that the atomic ratio of F^- to Nd^{3+} is $2.96 \pm 0.56:1$, close to the theoretical ratio of $3:1$ in NdF_3 (Figure S19, Supporting Information).

KF Alkali Metal Precursor. Having demonstrated how OAm stabilizes CsNd_2F_7 nanocrystals, we next turn our attention to changing the alkali metal fluoride to KF. In the absence of OAm ($R_0 = 0$), $R_M = 4$ and $T_r = 300\text{ }^\circ\text{C}$, ultrathin rectangular nanoplates with average length $\langle L \rangle = 86.9 \pm 51.0\text{ nm}$, width $\langle W \rangle = 32.5 \pm 11.7\text{ nm}$, and thickness $\langle l \rangle = 7.8 \pm 1.9\text{ nm}$ are obtained (Figure 6A and Figure S20, Supporting Information). The nanoplates exhibit diffraction peaks that match those of standard orthorhombic KNdF_4 (Figure 6C). Increasing R_0 to 0.4 results also in the formation of orthorhombic KNdF_4 nanocrystals, albeit with non-uniform shapes (Figure S21, Supporting Information). It is worth mentioning that when $R_0 = 0.4$, KNdF_4 nanoplates were previously reported when KOH and NH_4F were used as the alkali metal and fluoride precursors, respectively.¹⁰

When an excess amount of OAm ($R_0 = 1.6$) is introduced into the reaction mixture, the product obtained are uniformly distributed nanodiscs for $T_r = 300\text{ }^\circ\text{C}$ and $R_M = 4.0$ with

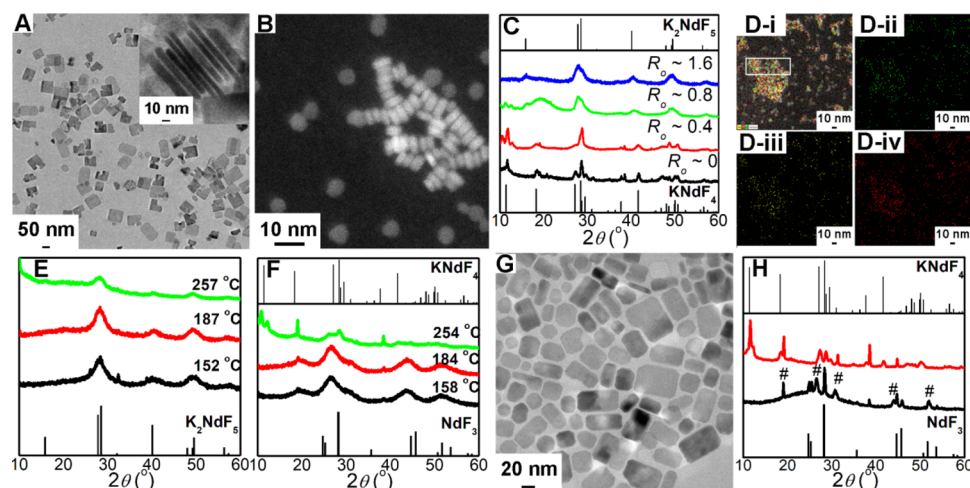


Figure 6. (A) TEM image of nanocrystals synthesized with KF as an alkali metal precursor, $R_M = 4$, $R_O = 0$, and $T_r = 300$ °C. Inset shows the TEM image of nanocrystals when stacked sideways, revealing the thickness of the nanoplates. (B) HAADF-STEM image of nanocrystals synthesized for $R_M = 4$, $R_O = 1.6$, and $T_r = 300$ °C. Nanodiscs lying either on their backs or sideways are observed. (C) XRD patterns of nanocrystals synthesized for $R_M = 4$, $T_r = 300$ °C, and different R_O values. (D) HAADF-STEM-correlated EDS elemental mapping images of K_2NdF_5 nanodiscs: (D-i) overlay of images from (ii), (iii), and (iv), (D-ii) K K-edge, (D-iii) Nd L-edge, and (D-iv) F K-edge. XRD patterns of nanocrystals synthesized for (E) $R_M = 4.0$, $R_O = 1.6$ (excess of OAm), and different T_r values and (F) $R_M = 4.0$, $R_O = 0$ (absence of OAm), and different T_r values. (G) TEM image and (H) XRD pattern (red) of nanocrystals obtained after heating K_2NdF_5 nanocrystals in a mixture of ODE (7 mL), OA (3 mL), and KF (1.6 mmol) at 300 °C for 120 min. The XRD pattern of nanocrystals obtained after heating K_2NdF_5 nanocrystals in a mixture of ODE (7 mL) and OA (3 mL) and without KF at 300 °C for 120 min is also given in (H) (black).

average diameter $\langle D \rangle = 5.9 \pm 0.9$ nm and thickness $\langle l \rangle = 2.3 \pm 0.3$ nm (Figure 6B and Figure S22, Supporting Information). The diffraction peaks of the nanodiscs are well indexed to those of standard hexagonal phase K_2NdF_5 (Figure 6C), suggesting that the ultrathin nanodisc consists of, at most, 2–3 unit cell layers (Text S3.3, Supporting Information). The chemical composition of the ultrathin K_2NdF_5 nanodiscs is further verified by HAADF-STEM-correlated EDS elemental mapping analysis of a group of nanodiscs highlighted in Figure 6D-i. The atomic ratio of $K^+ : Nd^{3+} : F^-$ is 20.4%:13.7%:65.8% (based on the boxed area in Figure 6D-i), in close agreement with the stoichiometric $K^+ : Nd^{3+} : F^-$ ratio in K_2NdF_5 (25%:12.5%:62.5%) (Figure S23, Supporting Information). The crystal growth of K_2NdF_5 nanodiscs occurs *via* cluster formation by fast random attachment of small nanocrystals followed by the breaking up of clusters to individual nanocrystals that subsequently grow with reaction time (Text S3.1, Supporting Information).

According to their XRD patterns in Figure 6E, hexagonal phase K_2NdF_5 nanocrystals are also formed at low ($T_r = 152$ and 187 °C) and intermediate ($T_r = 257$ °C) reaction temperatures when $R_O = 1.6$ (TEM images for $T_r = 187$ °C and 257 °C are given in Figure S24, Supporting Information). For $T_r = 152$ °C, the nanocrystals' atomic composition ratio from SEM-correlated EDS analysis is $K^+ : Nd^{3+} : F^- = 27.6 \pm 1.1\% : 14.7 \pm 2.1\% : 57.7 \pm 3.2\%$ (Figure S25, Supporting Information), supporting the formation of K_2NdF_5 . Therefore, K_2NdF_5 nanocrystals formed are thermodynamically stable in a non-acidic medium (e.g., $R_O = 1.6$). At an intermediate OAm concentration of $R_O = 0.8$, $R_M = 4.0$, and $T_r = 300$ °C, a mixture of $KNdF_4$ and K_2NdF_5 nanocrystals are observed (Figure 6C) (the TEM image of nanocrystals is given in Figure S26, Supporting Information).

Similar to the Cs ternary compounds, in an acidic environment, nanocrystals that are initially formed at low reaction temperatures undergo phase transformation when the

temperature is increased. For $R_M = 4.0$ and $R_O = 0$, the XRD patterns of the products recorded for $T_r = 158$ and 184 °C display broad peaks at $2\theta = 19.1, 26.4, 43.5$, and 51.3° (Figure 6F). Unfortunately, these peaks cannot be assigned exclusively to either standard hexagonal phase NdF_3 or other known potassium ternary fluoride compounds such as hexagonal/orthorhombic phase K_2NdF_5 (PDF no. 04-005-6011 for orthorhombic phase), orthorhombic phase $KNdF_4$, and K_3NdF_6 (PDF no. 00-040-0822). In order to establish the composition of the unknown product, HAADF-STEM-correlated EDS elemental analysis is applied, and the results for $R_O = 0$ and $T_r = 184$ °C are provided in Figure S27, Supporting Information. The atomic ratio of $K^+ : Nd^{3+} : F^-$, obtained by averaging eight randomly chosen areas ($125 \text{ nm} \times 125 \text{ nm}$ each), is $\sim 15.6 \pm 0.5\% : 14.2 \pm 0.7\% : 70.2 \pm 1.0\%$. When T_r is further increased to 254 °C, the XRD spectrum reveals that apart from the unknown product, $KNdF_4$ and potassium oleate (K-oleate) are also present (Figure 6F and Figure S28, Supporting Information). Finally, for $R_O = 0$ and $T_r = 300$ °C, the XRD pattern of the final product shows peaks that are indexed exclusively to orthorhombic $KNdF_4$ (Figure 6C).

Further insights into the thermodynamic stability of K_2NdF_5 nanocrystals in an acidic environment is investigated by redispersing an earlier prepared hexagonal phase K_2NdF_5 nanodiscs in a binary OA-ODE solvent and aged for 120 min at 300 °C. Compared to K_2NdF_5 nanodiscs, the morphology of the final product is rectangular-shaped nanocrystals with average length $\langle L \rangle = 15.7 \pm 1.5$ nm and width $\langle W \rangle = 13.8 \pm 0.3$ nm (Figure S29, Supporting Information). The XRD pattern reveals interesting features with peaks ascribed to NdF_3 along with additional well-defined peaks at $2\theta = 19.1, 26.4, 30.7, 44.0$, and 52.0° (marked with # in Figure 6H). Upon close examination, it is revealed that the diffraction peaks from NdF_3 and those labeled with # completely overlap with the broad peaks recorded for the

unknown product prepared in an acidic medium at low reaction temperatures (e.g., for $R_0 = 0$ and $T_r = 158/184$ °C in Figure 6F). Based on the HAADF-STEM-correlated EDS analysis results in Figure S27, Supporting Information, it is therefore speculated that the unknown product is most likely composed of a mixture of $K_{0.156}Nd_{0.142-y}F_{0.702-3y}$ and $y(NdF_3)$ ($y < 0.142$), and the diffraction peaks marked with # in Figure 6H belong to $K_{0.156}Nd_{0.142-y}F_{0.702-3y}$ nanocrystals whose crystallinity is markedly improved at high reaction temperatures. A diffraction peak at $2\theta = 38.4^\circ$ is also observed in Figure 6H, which is likely from a small amount of unremoved K-oleate during the washing process (Figures S17 and S28, Supporting Information). In a separate experiment, when K_2NdF_5 nanodiscs are redispersed in a binary OA-ODE solvent containing KF (1.6 mmol) and aged for 120 min at 300 °C, pure orthorhombic $KNdF_4$ nanoplates ($\langle L \rangle = 35.7 \pm 7.8$ nm and $\langle W \rangle = 26.0 \pm 7.5$ nm) are obtained instead (Figure 6G,H and Figure S30, Supporting Information). Therefore, K_2NdF_5 decomposes to $K_{0.156}Nd_{0.142-y}F_{0.702-3y}$ and $y(NdF_3)$ in the absence of KF in the solution and to $KNdF_4$ in the presence of KF.

In summary, $K_{0.156}Nd_{0.142-y}F_{0.702-3y}$ nanocrystals are formed *via* the decomposition of K_2NdF_5 nanocrystals in an acidic medium for either low reaction temperatures or high reaction temperatures in the absence of KF. This step is plausibly rapid, which renders the detection of K_2NdF_5 nanocrystals at low T_r when $R_0 = 0$ difficult. When a sufficient amount of KF is furnished, $KNdF_4$ nanocrystals are formed from a reaction that most likely involves $K_{0.156}Nd_{0.142-y}F_{0.702-3y}$, NdF_3 , KF, and OA at a high temperature. The exact mechanism is still unclear and remains to be fully elucidated at the present moment. Table S2, Supporting Information, provides a summary of the nanocrystals formed under various preparation conditions.

NaF Alkali Metal Precursor. The effects of environmental acidity on the phase of the product formed when NaF is used as the alkali metal precursor are also examined. In this case, cubic phase α - $NaNdF_4$ nanocrystals are obtained in a basic environment (e.g., $R_0 = 1.6$), whereas hexagonal phase β - $NaNdF_4$ nanocrystals are formed in an acidic medium (e.g., $R_0 = 0$ and 0.4) (Figure S31, Supporting Information). When α - $NaNdF_4$ nanocrystals are redispersed in a binary OA-ODE solvent and aged at 300 °C for 120 min, they are successfully converted to β - $NaNdF_4$ (Figure S31, Supporting Information). Therefore, the unstable α - $NaNdF_4$ nanocrystals undergo transformation to β - $NaNdF_4$ in an acidic medium at high temperatures. These results are in line with the observations reported by Naduviledathu Raj and co-workers.²¹

Downconversion Emission, Photothermal Conversion, and Computed Tomography. The downconversion emission, photothermal conversion, and computed tomography (CT) contrasting properties of the nanocrystals prepared with the reaction conditions $R_0 = 1.6$ and $T_r = 300$ °C are characterized by first transferring them to dimethylformamide (DMF) *via* ligand exchange with nitrosonium tetrafluoroborate ($NOBF_4$). The downconversion emission spectra, after NIR light (808 nm) excitation of the Nd^{3+} ions, display peaks at ~ 868 nm (${}^4F_{3/2} \rightarrow {}^4I_{9/2}$), ~ 1056 nm (${}^4F_{3/2} \rightarrow {}^4I_{11/2}$), and ~ 1319 nm (${}^4F_{3/2} \rightarrow {}^4I_{13/2}$) (Figure 7A). In this case, the absorbance at the excitation wavelength is ~ 0.043 for all samples (the absorption spectra are given in Figure S32, Supporting Information). The luminescence quantum yield (QY) increases in the following order: cubic phase $NaNdF_4 <$

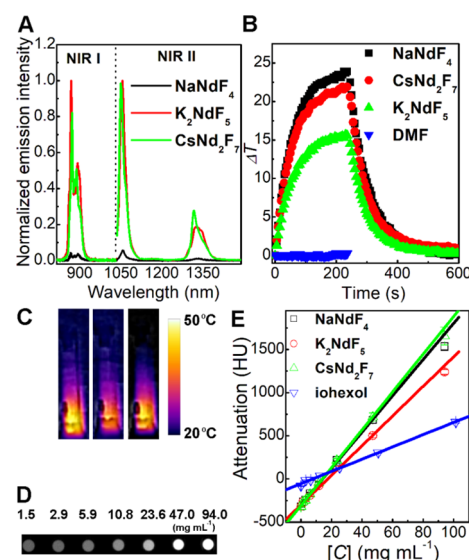


Figure 7. (A) Normalized emission spectra of orthorhombic phase $CsNd_2F_7$, hexagonal phase K_2NdF_5 , and cubic phase $NaNF_4$ nanocrystals in DMF solvent. The absorbances of the three samples at the excitation wavelength (808 nm) are kept similar (Figure S32, Supporting Information). (B) Temperature change profiles of DMF solutions of $CsNd_2F_7$, K_2NdF_5 , and $NaNF_4$ nanocrystals excited using an 808 nm laser for 240 s. The temperature change profile of the neat DMF solution is also given. (C) Corresponding thermal images taken after 240 s of light irradiation (from left to right: $NaNF_4$, K_2NdF_5 , and $CsNd_2F_7$ nanocrystals). (D) CT images of phantom containing different concentrations of $CsNd_2F_7$ nanodiscs in DMF. Exact concentrations (1.5–94.0 mg mL⁻¹) are given above each sample. (E) Linear regression plot of $NaNF_4$, K_2NdF_5 , and $CsNd_2F_7$ nanocrystals in DMF and iohexol in PBS. Each error bar is from measurements from three independent samples. Attenuation rates (AR) from the fitted slopes with corresponding best-fit R^2 values are presented in Table S4, Supporting Information.

orthorhombic phase $CsNd_2F_7 <$ hexagonal phase K_2NdF_5 with a QY ratio = 0.044:0.9:1.0.

The photoluminescence intensity depends on the crystal field symmetry, Nd^{3+} – Nd^{3+} distance, and the surface area-to-volume ratio (SA/V).⁹ We will briefly discuss the emission intensities of the nanocrystals in Figure 7A using available data in the literature. Being a light lanthanide ion, Nd^{3+} is easily polarizable.⁴¹ In addition, the electronic polarizability of alkali metal increases in the order of $Na^+ < K^+ < Cs^+$.⁴² Therefore, it is predicted that a smaller extent of electron cloud distortion occurs in nanocrystals containing Na^+ , leading to higher lattice field symmetry and lower luminescence efficiency (*vice versa* for nanocrystals with Cs^+ and K^+).⁴³ The distance between neighboring Nd^{3+} ions in a unit cell of $NaNF_4$ is fixed and estimated to be 3.76 Å, whereas the Nd^{3+} – Nd^{3+} displacement for a $CsNd_2F_7$ unit cell falls in the range between *ca.* 3.75 and 9.31 Å, respectively (Text S3.4, Supporting Information). In general, the shorter Nd^{3+} – Nd^{3+} distances in the former may lead to stronger cross-relaxation (CR) from (${}^4F_{3/2}$, ${}^4I_{15/2}$) to (${}^4I_{9/2}$, ${}^4I_{15/2}$), yielding a more effective non-radiative relaxation pathway. In terms of SA/V, surface relaxation pathways associated with surface ligand quenching, quenching of emitters on the surface by the surrounding solvent, and surface defects acting as emission quenching sites should be considered.⁴⁴ It has been reported that for small nanoparticles with a large SA/V, surface defect quenching is an important factor that gives rise to reduced luminescence.^{44,45}

It is interesting to note, however, that the hexagonal phase K_2NdF_5 nanodisc with the largest SA/V ratio exhibits the highest emission intensity ($\text{SA}/V = 0.54, 0.43, \text{ and } 1.55 \text{ nm}^{-1}$ for NaNdF_4 , CsNd_2F_7 , and K_2NdF_5 , respectively) (Text S3.3, Supporting Information). A plausible explanation to rationalize this odd observation is due to a compensation effect arising from a large number of Nd^{3+} ions on the sub-10 nm lateral and ultrathin vertical surfaces (i.e., $\sim 5.9 \text{ nm}$ diameter and 2–3 atomic layer thickness) of K_2NdF_5 when compared to a smaller fraction of surface lanthanide ions for larger nanocrystals (e.g., CsNd_2F_7 and NaNdF_4). The surface ions of K_2NdF_5 nanocrystal are not well paired and hence give rise to a reduced probability of CR interaction and inefficient non-radiative relaxation. This is also evident in the weaker photothermal conversion efficiency observed for K_2NdF_5 as discussed below. In addition, a nanocrystal with a higher fraction of surface emitters with lower site symmetry has been proposed to exhibit enhanced emission.²⁰ Since the fraction of Nd^{3+} on the surface of cuboid NaNdF_4 is only 44.1% compared to the majority of Nd^{3+} at the surface of a disc-shaped K_2NdF_5 nanocrystal (Text 3.3, Supporting Information), the higher fraction of surface emitters in K_2NdF_5 may result in higher luminescence. In terms of the shape effect, the preferred growth direction and d -space distance between crystal planes play a role; a nanocrystal whose shape offers a large fraction of crystal planes with short d -space distance would experience decreased interplane ion-ion distance and a more efficient cross-relaxation process.⁴⁶ It must be emphasized that in order to fully explain the discrepancy in emission intensity seen amongst the various nanocrystals, all of the above factors including contribution from lattice phonon energy should be considered.

NIR light excitation of Nd^{3+} ions followed by cross-relaxation between pairs of closely spaced Nd^{3+} gives rise to dissipated heat when the excited Nd^{3+} ions undergo non-radiative relaxation.^{11,12} Figure 7B,C shows the time-resolved photothermal response profiles and thermal images of DMF solutions containing, separately, α - NaNdF_4 nanoparticles, hexagonal phase K_2NdF_5 nanodiscs, and orthorhombic phase CsNd_2F_7 nanodiscs. The nanocrystals are excited using NIR laser excitation (808 nm, 5.6 W cm^{-2}) under ambient conditions, and the absorbance at the excitation wavelength is ~ 0.26 . After 240 s of light irradiation, the maximum change in temperature (ΔT) for NaNdF_4 , K_2NdF_5 , and CsNd_2F_7 are 23.9, 15.6, and 21.9°C , respectively. Upon turning off the light source, the temperature of each solution gradually returns to room temperature. The light-to-heat conversion efficiencies of NaNdF_4 , K_2NdF_5 , and CsNd_2F_7 nanocrystals are 27.1 ± 4.3 , 16.2 ± 1.5 , and $26.6 \pm 3.4\%$, respectively (Text S3.5, Supporting Information). In addition, the nanocrystals also exhibit good photothermal stability even after five continuous heating/cooling cycles as illustrated in Figure S33, Supporting Information.

We next evaluated the potential of utilizing NaNdF_4 , K_2NdF_5 , and CsNd_2F_7 nanocrystals as CT contrast agents. The X-ray mass attenuation coefficient $\mu\rho^{-1}$ of a material is dependent on the atomic number and the percentage of the various elements found in the compound. At 50 keV, the $\mu\rho^{-1}$ values of NaNdF_4 , K_2NdF_5 , and CsNd_2F_7 are 9.88, 7.67, and $11.85 \text{ cm}^2 \text{ g}^{-1}$, respectively (Table S3, Supporting Information). When compared to the iodine-based CT contrast agent, iohexol ($\mu\rho^{-1} = 5.86 \text{ cm}^2 \text{ g}^{-1}$ at 50 keV), the lanthanide-based compounds are expected to outperform it. CT imaging of the

CsNd_2F_7 nanodiscs at 50 kV voltage energy is shown in Figure 7D. The CT signal of the samples clearly increases with the concentration of nanocrystals $[C]$. Similar observations are also noted for NaNdF_4 and K_2NdF_5 nanocrystals, with CT attenuation, expressed as Hounsfield units (HU), linearly scaling with the $[C]$ for the Nd^{3+} -based nanocrystals and iohexol (i.e., concentration studied: 0 to 101 mg mL^{-1}) (Figure 7E). In addition, the attenuation rate (AR) from the fitted slope decreases in the following order: CsNd_2F_7 ($\text{AR} = 21.9 \pm 0.5 \text{ HU mL mg}^{-1}$) $>$ NaNdF_4 ($21.0 \pm 0.3 \text{ HU mL mg}^{-1}$) $>$ K_2NdF_5 ($17.1 \pm 0.2 \text{ HU mL mg}^{-1}$) $>$ iohexol ($7.1 \pm 0.1 \text{ HU mL mg}^{-1}$). The trend observed for the AR values is qualitatively similar to the order of the mass attenuation coefficients (Table S3, Supporting Information). In particular, the Nd^{3+} -based nanocrystals provide higher attenuation when compared to iohexol. The data also demonstrates the potential to increase CT attenuation rates and imaging contrast-to-noise ratios (CNR) at specific X-ray energies by modifying nanocrystal compositions with optimal $\mu\rho^{-1}$ values.

CONCLUSIONS

We have demonstrated the facile synthesis of orthorhombic phase CsNd_2F_7 and hexagonal phase K_2NdF_5 nanocrystals in a non-acidic medium by reacting MF ($M = \text{Cs}$ and K), $\text{Nd}(\text{CH}_3\text{CO}_2)_3$, oleic acid (OA), and 1-octadecene in the presence of oleylamine ligands (OAm). On the other hand, in an acidic environment where OAm is either absent or in low amounts, CsNd_2F_7 nanocrystals are formed at low reaction temperatures (T_r) but undergo decomposition to NdF_3 and Cs-oleate at higher T_r ($>200^\circ\text{C}$). K_2NdF_5 nanocrystals are also unstable in an acidic environment, displaying rapid transformation to a mixture of $\text{K}_{0.156}\text{Nd}_{0.142-y}\text{F}_{0.702-3y}$ and $y(\text{NdF}_3)$ ($y < 0.142$) nanocrystals at low T_r and orthorhombic phase KNdF_4 nanocrystals at high T_r . Therefore, by judiciously controlling the acidity of the reaction mixture via the addition of OAm, initially formed CsNd_2F_7 and K_2NdF_5 nanocrystals remain thermodynamically stable at high temperatures (e.g., $T_r = 300^\circ\text{C}$). This is also observed for α - NaNdF_4 nanocrystals, which remains stable in a non-acidic OA-OAm-ODE solvent but transforms to β - NaNdF_4 in an acidic medium (e.g., OA-ODE solvent) at high temperatures.

The as-synthesized CsNd_2F_7 and K_2NdF_5 nanocrystals exhibit light-to-heat conversion efficiencies (16–27%) that are comparable to other photothermal materials (e.g., Cu_{2-x}Se nanocrystals).⁴⁷ The CT attenuation of both penta- and heptafluoride nanocrystals are higher than iohexol when measured at lower X-ray energy. By converting these nanocrystals to biocompatible formats, they have potential as multimodal theranostics for photothermal imaging/therapy and CT imaging in preclinical and clinical applications.

EXPERIMENTAL SECTION

Materials. Neodymium(III) acetate hydrate ($\text{Nd}(\text{CH}_3\text{CO}_2)_3 \cdot x\text{H}_2\text{O}$, 99.9%), 1-octadecene (ODE, 90%), oleic acid (OA, 65%–88%), oleylamine (OAm, 70%), and nitrosonium tetrafluoroborate (NOBF_4) were purchased from Sigma-Aldrich. Methanol (HPLC grade), cyclohexane (HPLC grade), and dimethylformamide (DMF, HPLC grade) were purchased from Tedia. NaF ($>98.0\%$), KF ($>99.8\%$), and CsF were purchased from Sinopharm Chemical Reagent, J.T. Baker, and Fluorochem, respectively. Ethanol (analytical reagent grade), 1,1,2,2-tetrachloroethane (98%), and iohexol ($300 \text{ mg iodine mL}^{-1}$) were purchased from Fisher Chemical, Alfa Aesar, and GE Healthcare, respectively. All chemicals were used as received.

Synthesis and Characterization of Nanocrystals. Concentrations of OA and OAm from the commercially as-purchased chemicals were first quantified. An amount of 63.4 μL of OA or 65.8 μL of OAm from the commercial source was added into *ca.* 500 μL of CDCl_3 . 1,1,2,2-Tetrachloroethane (20 μL) was also added to act as an internal standard in the ^1H NMR measurement. The actual amount of OA/OAm in the as-received chemical was calculated using the ratio of the ^1H NMR peak of OA/OAm (~ 5.32 ppm) to the ^1H NMR peak of 1,1,2,2-tetrachloroethane (~ 5.95 ppm). The actual amounts of OA and OAm in the as-received chemicals were determined to be 3.39 and 2.84 mmol mL^{-1} (Figure S18, Supporting Information).

The synthesis of the nanocrystals is based on a co-precipitation method. Briefly, 0.4 mmol of $\text{Nd}(\text{CH}_3\text{CO}_2)_3 \cdot x\text{H}_2\text{O}$ was mixed with OA (1 to 3 mL) and 7 mL of ODE in a 50 mL round-bottom flask under continuous stirring. The mixture was heated to 100 $^\circ\text{C}$ to remove water and oxygen and further heated to 150 $^\circ\text{C}$ and maintained at that temperature for 1 h under a N_2 atmosphere. The mixture was then cooled to room temperature after which OAm and methanol solution containing MF ($\text{M} = \text{Na}, \text{K}, \text{or Cs}$) were added dropwise into the mixture. The amounts of OA and OAm were added such that the OAm mol %:OA mol % ratio (R_o) ranged from 0 to 1.6 (see Table S1, Supporting Information). The slurry mixture was heated to 50 $^\circ\text{C}$ under a N_2 flow and maintained for 30 min under a N_2 atmosphere. The mixture was subsequently heated to 100 $^\circ\text{C}$ to remove water and oxygen and further heated to reach different reaction temperatures (T_r) and maintained at that temperature under a N_2 atmosphere for 2 h. After the solution was cooled to room temperature, 10 mL of ethanol was added to precipitate the nanocrystals, which were then retrieved by centrifugation at 4000 rpm for 5 min. The nanocrystals were then redispersed in 4 mL of cyclohexane, followed by washing with 10 mL of ethanol. The as-prepared nanocrystals were separated by centrifugation (4000 rpm for 5 min) and redispersed in cyclohexane for further characterization.

Synthesis of Nd-(Oleate)₃. $\text{Nd}(\text{CH}_3\text{CO}_2)_3 \cdot x\text{H}_2\text{O}$ (0.4 mmol) was mixed with 3 mL of OA and 7 mL of ODE in a 50 mL round-bottom flask under continuous stirring. The mixture was heated to 100 $^\circ\text{C}$ to remove water and oxygen and further heated to 150 $^\circ\text{C}$ and maintained at that temperature for 1 h under a N_2 atmosphere. After the solution was cooled to room temperature, 10 mL of ethanol was added to precipitate the Nd-(oleate)₃ complex, which were then retrieved by centrifugation at 4000 rpm for 5 min. The Nd-(oleate)₃ complex was redispersed in 4 mL of cyclohexane followed by washing with 10 mL of ethanol. The complex was then separated by centrifugation (4000 rpm for 5 min) and redispersed in cyclohexane for further characterization.

Synthesis of M-Oleate ($\text{M} = \text{Cs}$ and K). MF (1.6 mmol; $\text{M} = \text{Cs}, \text{K}$) was mixed with 3 mL of OA and 7 mL of ODE in a 50 mL round-bottom flask under continuous stirring. The mixture was heated to 100 $^\circ\text{C}$ to remove water and oxygen and further heated to 300 $^\circ\text{C}$ and maintained at that temperature for 2 h under a N_2 atmosphere. After the solution was cooled to room temperature, 10 mL of ethanol was added to precipitate the product, which was then retrieved by centrifugation at 4000 rpm for 5 min. The product was subsequently redispersed in 4 mL of cyclohexane followed by washing with 10 mL of ethanol. The as-prepared product was separated by centrifugation (4000 rpm for 5 min) and redispersed in cyclohexane for further characterization.

Acid-Base Reaction between OA and OAm. A room temperature reaction between OA and OAm was performed by mixing OA and OAm in ~ 500 μL of CDCl_3 in ratios of $R_o = 0.16, 0.80$, and 1.60, and the ^1H NMR spectra of the samples were recorded.

Reaction solutions obtained after the synthesis of the nanocrystals for $R_M = 4.0$ and $T_r = 160$ $^\circ\text{C}$ ($R_o = 1.6$) and $R_M = 4.0$ and $T_r = 300$ $^\circ\text{C}$ ($R_o = 0, 0.16, 0.8$, and 1.6) were cooled to room temperature, and an internal standard (1 mL of 1,1,2,2-tetrachloroethane) was added. The solutions were centrifuged at 7800 rpm for 5 min to remove the nanocrystals, and the supernatant was collected. Samples used for ^1H NMR measurements were prepared by mixing the supernatant

solutions with CDCl_3 . The ^1H NMR spectra were measured using a Bruker Avance III 400 spectrometer.

Redispersion of CsNd_2F_7 , K_2NdF_5 , and NaNdF_4 Nanocrystals in an Acidic Medium. Hexagonal phase K_2NdF_5 nanodiscs, orthorhombic phase CsNd_2F_7 nanodiscs, and α - NaNdF_4 nanocrystals, prepared under the conditions $R_M = 4.0$, $R_o = 1.6$, and $T_r = 300$ $^\circ\text{C}$, were separately redispersed in OA (3 mL) and ODE (7 mL) in a 50-mL round-bottom flask under continuous stirring. The mixture was heated to 100 $^\circ\text{C}$ to remove water and oxygen and further heated to 300 $^\circ\text{C}$ and maintained at that temperature for 2 h under a N_2 atmosphere. After the solution was cooled to room temperature, 10 mL of ethanol was added to precipitate the nanocrystals. The nanocrystals were further separated by centrifugation at 4000 rpm for 5 min and redispersed in 4 mL of cyclohexane followed by washing with 10 mL of ethanol. The as-prepared nanocrystals were separated by centrifugation at 4000 rpm for another 5 min and redispersed in cyclohexane for further characterization. In a separate experiment, K_2NdF_5 nanodiscs were redispersed in a mixture of OA (3 mL), ODE (7 mL), and KF (1.6 mmol) under continuous stirring, and the solution was treated as described above.

XRD, TEM, HAADF-STEM Imaging and Correlated EDS Elemental Mapping, SEM Imaging, and Correlated EDS Characterization. X-ray diffraction (XRD) patterns of nanocrystals were measured using a Bruker D8 Advance XRD diffractometer with $\text{Cu K}\alpha$ radiation. Transmission electron microscopy (TEM) images of nanocrystals were measured using a JEM-1400 electron microscope (JEOL). High-resolution TEM (HRTEM) images were obtained using a JEM-2100F electron microscope (JEOL). High-angle annular dark field scanning transmission electron microscopy images (HAADF-STEM) and the correlated energy-dispersive X-ray spectroscopy (EDS) analysis were measured using a JEM-2100F electron microscope (JEOL) attached with an Ultim Max TLE detector (Oxford Instruments). Scanning electron microscopy (SEM) images were obtained using a JEOL-JSM-7600F scanning electron microscope (JEOL), and elemental composition of the nanocrystals was determined using an EDS instrument (Oxford Instruments) attached to the JEOL-JSM-7600F SEM system.

Emission, Photothermal, and CT Imaging. OA-capped or OA/OAm-capped nanocrystals were first transferred to DMF. Cyclohexane solution (4 mL) of the as-prepared OA-capped or OA/OAm-capped nanocrystals was mixed with DMF (5 mL) solution of NOBF₄ (20 mM). The mixture was stirred at room temperature for 30 min, and the solution in the DMF layer was collected and centrifuged at 14,000 rpm for 30 min. The collected nanocrystals after centrifugation were washed with a mixture of cyclohexane/DMF (1:1) twice and redispersed in DMF for further analysis.

The UV–visible absorption spectra of the nanocrystals in DMF were measured using a UV–visible spectrophotometer (Cary 100, Varian). The NIR emission spectra were measured using a home-built setup with an 808 nm DPSS laser (4.2 W cm^{-2} , VA-1-DC-808, Beijing Viasho Technology). An AvaSpec-ULS2048 (Avantes) detector was used to record luminescence between 820 and 1035 nm (labeled as “NIR I” in Figure 7A) and an AvaSpec-NIR256–1.7TEC (Avantes) detector for luminescence >1035 nm (labeled as “NIR II” in Figure 7A).

The light-to-heat conversion efficiency of the nanocrystals in DMF (200 μL) was measured in a quartz cuvette (optical path ≈ 0.5 cm and OD ≈ 0.26 at 808 nm). The solution was irradiated with an 808 nm laser light (5.6 W cm^{-2}) (MDL-H-808-2.5W, Changchun New Industries Optoelectronics Technology), and the temperature increase was measured using a thermal imaging camera (FLIR E5, FLIR Systems).

Computed tomography (CT) phantoms were created by loading PCR tubes with serial dilutions of CsNd_2F_7 , K_2NdF_5 , and NaNdF_4 nanocrystals (concentrations from 0 to 94.0 mg mL^{-1} in 50 μL of DMF) and iohexol (concentrations from 0 to 101.0 mg mL^{-1} in 50 μL of PBS (phosphate buffered saline)). Phantoms were scanned in the VECTOr³CT (MILabs), which uses cone-beam CT geometry with a high-resolution CMOS detector (1536 \times 1944 pixels). CT was performed at 50 kV (0.19 mA) with the following parameters: full

rotation (360°) acquisition with a step-angle of 0.5° (720 total projections) and 0.75 ms exposure time. Volumetric CT image data was reconstructed using a 3D Feldkamp filtered back-projection (FBP) algorithm (MILabs) to an isotropic voxel size of 80 μm . Volumes-of-interest (VOIs) were defined on the CT images and quantified in PMOD v3.8 (Bruker) to calculate the average image radiodensity, expressed as a CT attenuation value in Hounsfield units (HU), calibrated to air (−1000 HU) and water (0 HU).

■ ASSOCIATED CONTENT

SI Supporting Information

The Supporting Information is available free of charge at <https://pubs.acs.org/doi/10.1021/acs.chemmater.1c02736>.

Additional TEM, HRTEM, HAADF-STEM correlated EDS, SEM correlated EDS, ^1H NMR spectra, UV–visible absorption spectra, size distributions, tables and texts on crystal growth, determination of the amount of unreacted OA remaining in the reaction mixture, determination of thickness of the K_2NdF_5 nanodisc and the surface area-to-volume ratio of nanocrystals, determination of the photothermal conversion efficiency and estimation of Nd^{3+} – Nd^{3+} separation in NaNdF_4 and CsNd_2F_7 (PDF)

■ AUTHOR INFORMATION

Corresponding Author

Edwin K. L. Yeow – Division of Chemistry and Biological Chemistry, School of Physical and Mathematical Sciences, Nanyang Technological University, 637371, Singapore; orcid.org/0000-0003-0290-4882; Email: edwinyeow@ntu.edu.sg

Authors

Xiangyang Wu – Division of Chemistry and Biological Chemistry, School of Physical and Mathematical Sciences, Nanyang Technological University, 637371, Singapore
Jing Yang Tham – Laboratory for Translational and Molecular Imaging, Cancer and Stem Cell Biology Programme, Duke-NUS Medical School, 169857, Singapore
Ann-Marie Chacko – Laboratory for Translational and Molecular Imaging, Cancer and Stem Cell Biology Programme, Duke-NUS Medical School, 169857, Singapore; orcid.org/0000-0001-5140-2622

Complete contact information is available at: <https://pubs.acs.org/doi/10.1021/acs.chemmater.1c02736>

Author Contributions

The manuscript was written through contributions of all authors. All authors have given approval to the final version of the manuscript.

Funding

We acknowledge financial support from the Singapore Ministry of Education MoE Tier 1 grants (RG89/20 and RG6/18) and Duke-NUS Block Grant.

Notes

The authors declare no competing financial interest.

■ REFERENCES

- (1) Wen, S.; Zhou, J.; Zheng, K.; Bednarkiewicz, A.; Liu, X.; Jin, D. Advances in Highly Doped Upconversion Nanoparticles. *Nat. Commun.* **2018**, *9*, 2415.
- (2) Zhang, Z.; Han, Q.; Lau, J. W.; Xing, B. Lanthanide-Doped Upconversion Nanoparticles Meet Cutting-Edge Bioapplications:

Recent Progress and Perspectives. *ACS Materials Lett.* **2020**, *2*, 1516–1531.

(3) Wilhelm, S. Perspectives for Upconverting Nanoparticles. *ACS Nano* **2017**, *11*, 10644–10653.

(4) Yu, Z.; Chan, W. K.; Tan, T. T. Y. Neodymium-Sensitized Nanoconstructs for Near-Infrared Enabled Photomedicine. *Small* **2020**, *16*, 1905265.

(5) del Rosal, B.; Rocha, U.; Ximendes, E. C.; Martín Rodríguez, E.; Jaque, D.; García Solé, J. Nd^{3+} Ions in Nanomedicine: Perspectives and Applications. *Opt. Mater.* **2017**, *63*, 185–196.

(6) Hudson, D. E.; Hudson, D. O.; Wininger, J. M.; Richardson, B. D. Penetration of Laser Light at 808 nm and 980 nm in Bovine Tissue Samples. *Photomed. Laser Surg.* **2013**, *31*, 163–168.

(7) Xie, X.; Gao, N.; Deng, R.; Sun, Q.; Xu, Q.-H.; Liu, X. Mechanistic Investigation of Photon Upconversion in Nd^{3+} -sensitized Core-Shell Nanoparticles. *J. Am. Chem. Soc.* **2013**, *135*, 12608–12611.

(8) Du, Q.; Wu, X.; Bi, W.; Xing, B. G.; Yeow, E. K. L. Increasing Antibiotic Activity by Rapid Bioorthogonal Conjugation of Drug to Resistant Bacteria Using an Upconverted Light-Activated Photocatalyst. *J. Mater. Chem. B* **2021**, *9*, 3136–3142.

(9) Wu, X.; Yeow, E. K. L. Tuning the NIR Downconversion Luminescence and Photothermal Conversion Efficiencies of $\text{MNd}_x\text{Y}_{1-x}\text{F}_4$ ($\text{M} = \text{Na}$ and Li) Nanocrystals for Use in Anti-Counterfeiting Labels With Opposite Displays. *Nanoscale* **2019**, *11*, 15259–15269.

(10) Wu, X.; Yeow, E. K. L. Ultrathin Near-Infrared Light Activated Nano-Hotplate Catalyst. *Small* **2020**, *16*, 2002698.

(11) Badnarkiewicz, A.; Wawrzynczyk, D.; Nyk, M.; Strek, W. Optically Stimulated Heating Using Nd^{3+} Doped NaYF_4 Colloidal Near Infrared Nanophosphors. *Appl. Phys. B: Lasers Opt.* **2011**, *103*, 847–852.

(12) Wawrzynczyk, D.; Badnarkiewicz, A.; Nyk, M.; Strek, W.; Samoc, S. Neodymium(III) Doped Fluoride Nanoparticle as Non-Contact Optical Temperature Sensors. *Nanoscale* **2012**, *4*, 6959–6961.

(13) Ding, L.; Ren, F.; Liu, Z.; Jiang, Z.; Yun, B.; Sun, Q.; Li, Z. Size-Dependent Photothermal Conversion and Photoluminescence of Theranostic NaNdF_4 Nanoparticles under Excitation of Different Wavelength Lasers. *Bioconjugate Chem.* **2020**, *31*, 340–351.

(14) Liu, X.; Ai, K.; Liu, J.; Yuan, Q.; He, Y.; Lu, L. A High Performance Ytterbium-Based Nanoparticulate Contrast Agent for In Vivo X-Ray Computed Tomography Imaging. *Angew. Chem., Int. Ed.* **2012**, *51*, 1437–1442.

(15) Zhang, G.; Liu, Y.; Yuan, Q.; Zong, C.; Liu, J.; Lu, L. Dual Mode In Vivo Imaging Using Upconversion Luminescence and Enhanced Computed Tomography Properties. *Nanoscale* **2011**, *3*, 4365–4371.

(16) Tian, G.; Zheng, X.; Zhang, X.; Yin, W.; Yu, J.; Wang, D.; Zhang, Z.; Yang, X.; Gu, Z.; Zhao, Y. TPGS-Stabilized $\text{NaYbF}_4:\text{Er}$ Upconversion Nanoparticles for Dual-Modal Fluorescent/CT Imaging and Anticancer Drug Delivery to Overcome Multi-Drug Resistance. *Biomaterials* **2015**, *40*, 107–116.

(17) Cruje, C.; Dunmore-Buyze, J.; MacDonald, J. P.; Holdsworth, D. W.; Drangova, M.; Gillies, E. R. Polymer Assembly Encapsulation of Lanthanide Nanoparticles as Contrast Agents for In Vivo Micro-CT. *Biomacromolecules* **2018**, *19*, 896–905.

(18) Ma, J.; Huang, P.; He, M.; Pan, L.; Zhou, Z.; Feng, L.; Gao, G.; Cui, D. Folic Acid-Conjugated $\text{LaF}_3:\text{Yb},\text{Tm}@/\text{SiO}_2$ Nanoparticles for Targeting Dual-Modality Imaging of Upconversion Luminescence and X-Ray Computed Tomography. *J. Phys. Chem. B* **2012**, *116*, 14062–14070.

(19) Liu, Y.; Li, L.; Guo, Q.; Wang, L.; Liu, D.; Wei, Z.; Zhou, J. Novel Cs-Based Upconversion Nanoparticles as Dual-Modal CT and UCL Imaging Agents for Chemo-Photothermal Synergistic Therapy. *Theranostics* **2016**, *6*, 1491–1505.

(20) Mai, H.-X.; Zhang, Y.-W.; Si, R.; Yan, Z.-G.; Sun, L.-D.; You, L.-P.; Yan, C.-H. High-Quality Sodium Rare-Earth Fluoride Nanocrystals: Controlled Synthesis and Optical Properties. *J. Am. Chem. Soc.* **2006**, *128*, 6426–6436.

- (21) Naduviledathu Raj, A.; Rinkel, T.; Haase, M. Ostwald Ripening, Particle Size Focusing, and Decomposition of Sub-10 nm NaREF₄ (RE = La, Ce, Pr, Nd) Nanocrystals. *Chem. Mater.* **2014**, *26*, 5689–5694.
- (22) Chen, B.; Ren, B.; Wang, F. Cs⁺-Assisted Synthesis of NaLaF₄ Nanoparticles. *Chem. Mater.* **2019**, *31*, 9497–9503.
- (23) Chen, B.; Kong, W.; Wang, N.; Zhu, G.; Wang, F. Oleylamine-Mediated Synthesis of Small NaYbF₄ Nanoparticles with Tunable Size. *Chem. Mater.* **2019**, *31*, 4779–4786.
- (24) Rastogi, C. K.; Lu, E.; Tam, J.; Pichaandi, J. M.; Howe, J.; Winnik, M. A. Influence of the Sodium Precursor on the Cubic-to-Hexagonal Phase Transformation and Controlled Preparation of Uniform NaNdF₄ Nanoparticles. *Langmuir* **2021**, *37*, 2146–2152.
- (25) Zeng, S.; Ren, G.; Xu, C.; Yang, Q. High Uniformity and Monodispersity of Sodium Rare-Earth Fluoride Nanocrystals: Controllable Synthesis, Shape Evolution and Optical Properties. *CrystEngComm* **2011**, *12*, 1384–1390.
- (26) Xu, L.; Li, J.; Wen, S.; Chen, H.; Shahzad, M. K.; Zhao, E.; Li, H.; Ren, J.; Zhang, J.; Liu, L. Sub-10 nm NaNdF₄ Nanoparticles as Near-Infrared Photothermal Probes with Self-Temperature Feedback. *ACS Appl. Nano Mater.* **2020**, *3*, 2517–2526.
- (27) Demianets, L. N. Hydrothermal Synthesis of New Compounds. *Prog. Cryst. Growth Charact. Mater.* **1990**, *21*, 299–355.
- (28) Friese, K.; Khaidukov, N.; Grzechnik, A. Twinned CsLn₂F₇ Compounds (Ln = Nd, Gd, Tb, Er, Yb): The Role of a Highly Symmetrical Cation Lattice with an Arrangement Analogous to the Laves Phase MgZn₂. *Z. Kristallogr.* **2016**, *231*, 631–639.
- (29) Pierrard, A.; Gredin, P.; De Kozak, A.; Viana, B.; Aschehoug, P.; Vivien, D.; Derouet, J.; Bourée-Vigneron, F. Structural Characterization of KLa₂F₇ and Spectroscopic Study of KLa₂F₇:Nd³⁺. *Phys. Status Solidi B* **2001**, *226*, 329–338.
- (30) de Barros, C. L. M.; Barthém, R. B.; Khaidukov, N. M. Optical Excitation of Nd³⁺ Pairs in CsGd₂F₇ Crystals. *J. Lumin.* **1999**, *82*, 307–314.
- (31) Wang, S.; Lin, J.; He, Y.; Chen, J.; Yang, C.; Huang, F.; Chen, D. Remarkable Laser-Driven Upconverting Photothermal Effect of Cs₃LnF₆@glass Nanocomposites for Anti-Counterfeiting. *Chem. Eng. J.* **2020**, *394*, 124889.
- (32) Fedorov, P. P. Systems of Alkali and Rare-Earth Metal Fluorides. *Russ. J. Inorg. Chem.* **1999**, *44*, 1703–1727.
- (33) Kim, J.; Bar-Ness, D.; Si-Mohamed, S.; Coulon, P.; Blevis, I.; Douek, P.; Cormode, D. P. Assessment of Candidate Elements for Development of Spectral Photon-Counting CT Specific Contrast Agents. *Sci. Rep.* **2018**, *8*, 12119.
- (34) Si-Mohamed, S.; Bar-Ness, D.; Sigovan, M.; Cormode, D. P.; Coulon, P.; Coche, E.; Vlassenbroek, A.; Normand, G.; Boussel, L.; Douek, P. Review of an Initial Experience with an Experimental Spectral Photon-Counting Computed Tomography System. *Nucl. Instrum. Methods Phys. Res., Sect. A* **2017**, *873*, 27–35.
- (35) Niu, W.; Wu, S.; Zhang, S. Utilizing the Amidation Reaction to Address the “Cooperative Effect” of Carboxylic Acid/Amine on the Size, Shape, and Multicolor Output of Fluoride Upconversion Nanoparticles. *J. Mater. Chem.* **2011**, *21*, 10894–10902.
- (36) Ostrowski, A. D.; Chan, E. M.; Gargas, D. J.; Katz, E. M.; Han, G.; Schuck, P. J.; Milliron, D. J.; Cohen, B. E. Controlled Synthesis and Single-Particle Imaging of Bright, Sub-10 nm Lanthanide-Doped Upconverting Nanocrystals. *ACS Nano* **2012**, *6*, 2686–2692.
- (37) Almeida, G.; Goldoni, L.; Akkerman, Q.; Dang, Z.; Khan, A. H.; Marras, S.; Moreels, I.; Manna, L. Role of Acid-Base Equilibria in the Size, Shape, and Phase Control of Cesium Lead Bromide Nanocrystals. *ACS Nano* **2018**, *12*, 1704–1711.
- (38) Shi, Y.; Larsson, R. Non-Corrosive and Biomaterials Protic Ionic Liquids with High Lubricating Performance. *Tribol. Lett.* **2016**, *63*, 1.
- (39) Shih, L.; Chung, Y.; Sriram, R.; Jue, T. Interaction of Myoglobin with Oleic Acid. *Chem. Phys. Lipids* **2015**, *191*, 115–122.
- (40) Wu, H.; Yang, Y.; Cao, Y. C. Synthesis of Colloidal Uranium-Dioxide Nanocrystals. *J. Am. Chem. Soc.* **2006**, *128*, 16522–16523.
- (41) Damasco, J. A.; Chen, G.; Shao, W.; Ågren, H.; Huang, H.; Song, W.; Lovell, J. F.; Prasad, P. N. Size-Tunable and Monodisperse Tm³⁺/Gd³⁺-Doped Hexagonal NaYbF₄ Nanoparticles with Engineered Efficient Near Infrared-to-Near Infrared Upconversion for In Vivo Imaging. *ACS Appl. Mater. Interfaces* **2014**, *6*, 13884–13893.
- (42) Shannon, R. D.; Fischer, R. X. Empirical Electronic Polarizabilities of Ions For the Prediction and Interpretation of Refractive Indices: Oxides and Oxysalts. *Am. Mineral.* **2016**, *101*, 2288–2300.
- (43) Li, Y.; Liu, C.; Zhang, P.; Huang, J.; Ning, H.; Xiao, P.; Hou, Y.; Jing, L.; Gao, M. Doping Lanthanide Nanocrystals With Non-lanthanide Ions to Simultaneously Enhance Up- and Down-conversion Luminescence. *Front. Chem.* **2020**, *8*, 832.
- (44) Zhao, J.; Lu, Z.; Yin, Y.; McRae, C.; Piper, J. A.; Dawes, J. M.; Jin, D.; Goldys, E. M. Upconversion Luminescence with Tunable Lifetime in NaYF₄:Yb,Er Nanocrystals: Role of Nanocrystal Size. *Nanoscale* **2013**, *5*, 944–952.
- (45) Xue, X.; Uechi, S.; Tiwari, R. N.; Duan, Z.; Liao, M.; Yoshimura, M.; Suzuki, T.; Ohishi, Y. Size-Dependent Upconversion Luminescence and Quenching Mechanism of LiYF₄:Er³⁺/Yb³⁺ Nanocrystals with Oleate Ligand Adsorbed. *Opt. Mater. Express* **2013**, *3*, 989–999.
- (46) Shan, J.; Uddi, M.; Wei, R.; Yao, N.; Ju, Y. The Hidden Effects of Particle Shape and Criteria for Evaluating the Upconversion Luminescence of the Lanthanide Doped Nanophosphors. *J. Phys. Chem. C* **2010**, *114*, 2452–2461.
- (47) Hessel, C. M.; Pattani, V. P.; Rasch, M.; Panthani, M. G.; Koo, B.; Tunnell, J. W.; Korgel, B. A. Copper Selenide Nanocrystals for Photothermal Therapy. *Nano Lett.* **2011**, *11*, 2560–2566.